Supplementary Information for "Solving the Trivial Crossing Problem While Preserving the Nodal Symmetry of the Wavefunction"

Elizabeth M. Y. Lee and Adam P. Willard*

(Dated: June 15, 2019)

CONTENTS

S.1. DERIVATION OF THE DIABATIC MIXING ANGLE

We diagonalize the diabatic Hamiltonian,

$$\mathbf{H} = \begin{bmatrix} E_a & V_{ab} \\ V_{ab} & E_b \end{bmatrix}, \tag{S.1}$$

by a unitary matrix,

$$\mathbf{U} = \begin{bmatrix} \cos\frac{\tau}{2} & \sin\frac{\tau}{2}, \\ -\sin\frac{\tau}{2} & \cos\frac{\tau}{2} \end{bmatrix}, \tag{S.2}$$

such that the following holds true:

$$\mathbf{U}^{-1}\mathbf{H}\mathbf{U} = \begin{bmatrix} \lambda_1 & 0 \\ 0 & \lambda_2 \end{bmatrix}. \tag{S.3}$$

Here λ_1 and λ_2 are eigenvalues of the quantum Hamiltonian. The corresponding eigenstates are

$$|\Psi_1\rangle = \cos\frac{\tau}{2}|\phi_a\rangle + \sin\frac{\tau}{2}|\phi_b\rangle, \tag{S.4}$$

$$|\Psi_2\rangle = -\sin\frac{\tau}{2}|\phi_a\rangle + \cos\frac{\tau}{2}|\phi_b\rangle, \tag{S.5}$$

where

$$\tau[\mathbf{x}(t)] = \arctan\frac{2V_{ab}[\mathbf{x}(t)]}{E_a[\mathbf{x}(t)] - E_b[\mathbf{x}(t)]}, \tag{S.6}$$

is the mixing angle between the diabatic states.

S.2. ENERGY GAP FOR NON-ORTHOGONAL BASIS

For a two level system as shown in Eq. 3 in the main text, the adiabatic energy gap for non-orthogonal basis states is given as

$$\lambda_2 - \lambda_1 = \frac{\sqrt{(E_a - E_b)^2 + 4V_{ab}^2 + 4f(S)}}{1 - S^2}, \tag{S.7}$$

where $S \equiv \langle\phi_a|\phi_b\rangle = \int \phi_a(\mathbf{r})^*\phi_b(\mathbf{r})d\mathbf{r}$ for $\mathbf{r} \in \mathbb{R}^3$ and $f(S) \equiv S^2E_aE_b - SV_{ab}(E_a + E_b)$. In order for the diabatic coupling to be physically meaningful, the diabatic states must be orthogonal.[1] Hence, we will focus on cases with orthonormal diabatic states, where $S = 0$, and thus Eq. S.7 simplifies to

$$\lambda_2 - \lambda_1 = \sqrt{(E_a - E_b)^2 + 4V_{ab}^2}, \tag{S.8}$$

which is the same equation as Eq. 7 in the main text.

S.3. SYMMETRY PRESERVING ADIABATIC DYNAMICS

A. Multi-state symmetry preserving method for nested trivial crossings

In a multi-state system, there is a possibility of additional trivial crossings during a given trivial crossing period, which we refer to as *nested trivial crossings*. We use the convention, $t_{\rm c}^{(1)} < t_{\rm c}^{(2)} < \cdots < t_{\rm c}^{(n)} < t_{\rm r}^{(n)} < \cdots < t_{\rm r}^{(2)} < t_{\rm r}^{(1)}$, to define n-number of nested trivial crossing periods. For example, consider a three-level system described as

$$\hat{H} = \hat{H}_a + \hat{H}_b + \hat{V}_{ab} + \hat{H}_c + \hat{V}_{ac} + \hat{V}_{bc}. \tag{S.9}$$

If there is a trivial crossing occurring first between states $|\phi_a\rangle$ and $|\phi_b\rangle$, we eliminate $|\phi_b\rangle$ by applying a switching function as follows:

$$\hat{H}_{\rm mod}^{(1)}(t) = \hat{H}_a + f_b^{(1)}(t)[\hat{H}_b + \hat{V}_{ab} + \hat{V}_{bc}] + \hat{H}_c + \hat{V}_{ac}, \tag{S.10}$$

where

$$f_b^{(1)}(t) = \begin{cases} 0 & \text{if } |V_{ab}| \leq V_{\rm c} \text{ and } t_{\rm c}^{(1)} \leq t \leq t_{\rm r}^{(1)}, \\ 1 & \text{otherwise.} \end{cases} \tag{S.11}$$

If there is another trivial crossing between the states a and c within the modified Hamiltonian $\hat{H}_{\rm mod}^{(1)}$, we apply an additional switching function for state c to eliminate both states b and c from the original Hamiltonian $\hat{H}$, *i.e.*,

$$\hat{H}_{\rm mod}^{(2)}(t) = \hat{H}_a + f_b^{(1)}(t)[\hat{H}_b + \hat{V}_{ab} + \hat{V}_{bc}] + f_c^{(2)}(t)[\hat{H}_c + \hat{V}_{ac}], \tag{S.12}$$

where

$$f_c^{(2)}(t) = \begin{cases} 0 & \text{if } |V_{ac}| \leq V_{\rm c} \text{ and } t_{\rm c}^{(2)} \leq t \leq t_{\rm r}^{(2)}, \\ 1 & \text{otherwise.} \end{cases} \tag{S.13}$$

Similar to the switching function algorithm, the energetic bias algorithm for nested trivial crossings works as follows:

$$\hat{H}_{\rm mod}^{(2)}(t) = \hat{H}_a + [\hat{H}_b + \sum_{i\in b} \Delta_0 |i\rangle\langle i|] + \hat{V}_{ab} + \hat{V}_{bc} + [\hat{H}_c + \sum_{i\in c} \Delta_0 |i\rangle\langle i|] + \hat{V}_{ac}, \tag{S.14}$$

where Δ_0 is a constant that raises the energy levels of basis states $|i\rangle$ belonging to diabatic states $|\phi_b\rangle$ and $|\phi_c\rangle$.

In both algorithms, let $|\Psi_1^{(\mathrm{mod,k})}\rangle$ be the lowest eigenstate of the modified Hamiltonian $\hat{H}_{\mathrm{mod}}^{(k)}$ where $k = 0$ is the original Hamiltonian ($\hat{H}_{\mathrm{mod}}^{(0)} \equiv \hat{H}$). The modified Hamiltonian has the property that $|\langle\Psi_1^{(\mathrm{mod,k})}(t)|\Psi_1^{(\mathrm{mod,k-1})}(t)\rangle| \approx 0.5$ at $t = t_{\mathrm{c}}^{(k)}$ and $|\langle\Psi_1^{(\mathrm{mod,k})}(t)|\Psi_1^{(\mathrm{mod,k-1})}(t)\rangle| \approx 1$ at $t = t_{\mathrm{r}}^{(k)}$. Our multi-state symmetry preserving method is summarized in Figure 3 (main text).

B. Choice of trivial recrossing threshold S_{c}

Transport properties of excitons are insensitive to the choice of S_{c} as long as it is chosen to be reasonably close to 1. For example, Figure S.1 shows that the average steady state diffusivity of excitons is independent of the choice of S_{c} for $S_{\mathrm{c}} > 0.7$. The uncertainty in the diffusivity generally decreases with increasing S_{c}. Hence, we have chosen $S_{\mathrm{c}} = 0.99$ for all simulations in the polythiophene example.

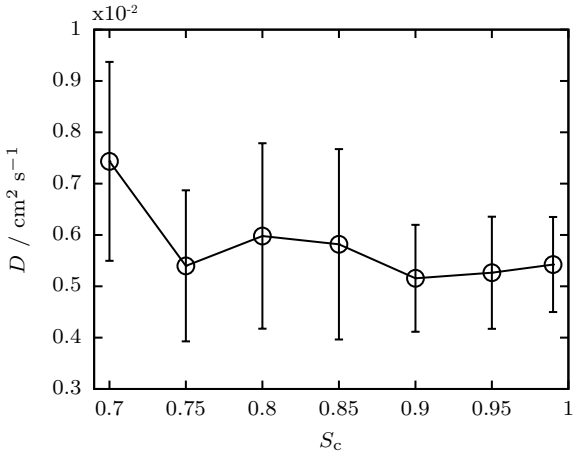

FIG. S.1. Dependence of diffusivity, D, on S_{c} in the symmetry preserving method. Statistics are taken for lowest exciton state trajectories on 100-monomer linear chains using $V_{\mathrm{c}} = 5$ meV. Error bars denote one standard deviation uncertainty among 10 samples, each averaged over 500 independent trajectories.

C. Comparison between switching function and energetic shift algorithms

Figure S.2 compares two algorithms that simulate symmetry preserving adiabatic dynamics: switching function and energetic bias. As long as the energy shift constant, Δ_0, is

larger than the magnitude of the largest off-diagonal element in the original Hamiltonian (in this case about 0.1 eV), we find that the potential energy surface of the active state is energetically well separated from higher energy potential energy surfaces that cause trivial crossing problems. Switching function and energetic bias algorithms result in the same adiabatic dynamics, as seen by identical red curves in the figure. Moreover, the active state computed by both methods is the lowest exciton state that has non-negative wavefunction amplitudes throughout the entire simulation.

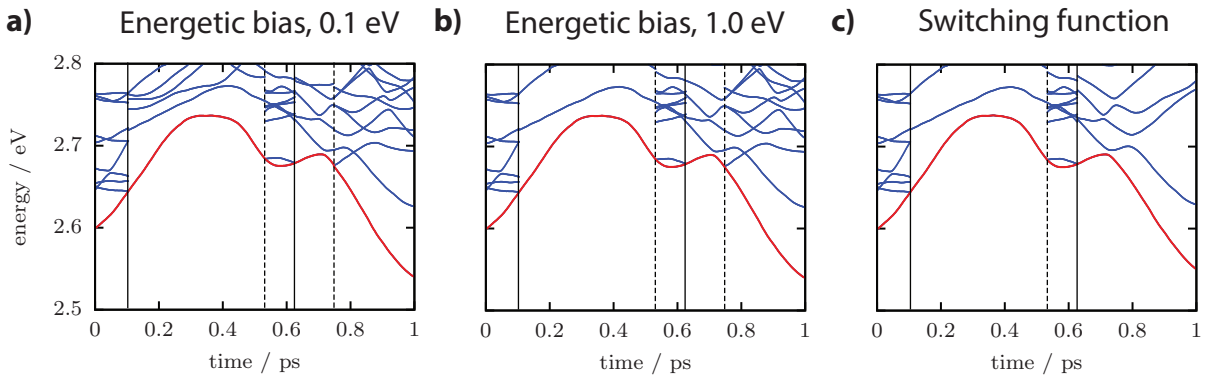

FIG. S.2. Time dependence of the excited state energy levels of the lowest eigenstates from two algorithms of the symmetry preserving method: energetic bias and switching function. (a) Energetic bias with $\Delta_0 = 0.1$ eV. (b) Energetic bias with $\Delta_0 = 1.0$ eV. (c) Switching function. Solid vertical lines mark the time when the Hamiltonian is modified in response to a trivial crossing. Dashed line indicates the point when the trivial crossing problem vanishes and the Hamiltonian is restored to its original unmodified form. All trajectories are initialized from identical configurations. They follow the same adiabatic dynamics, indicated by identical red curves. Initial configurations used to generate this figure are the same as those used to plot Figure 5 in the main text.

S.4. SIGN CHANGES AND PHASE CONSERVATION UPON TRIVIAL CROSSING

Consider two eigenstates, $|\Psi_1\rangle$ and $|\Psi_2\rangle$, that are superpositions of two orthonormal diabatic states, $|\phi_a\rangle$ and $|\phi_b\rangle$, at the vicinity of trivial crossing:

$$|\Psi_1(t)\rangle = c_a^{(1)}(t)|\phi_a\rangle + c_b^{(1)}(t)|\phi_b\rangle, \tag{S.15}$$

$$|\Psi_2(t)\rangle = c_a^{(2)}(t)|\phi_a\rangle + c_b^{(2)}(t)|\phi_b\rangle. \tag{S.16}$$

Let $|\Psi_1\rangle$ be the active adiabatic state throughout the adiabatic dynamics simulation that is initialized in the diabatic state $|\phi_a\rangle$. In practice, signs of coefficients for eigenstates coming out of numerical eigensolver (in our case, we used Eigen library for C++ code) are random. To conserve the phase of the active diabat during adiabatic simulations, we need to account for sign changes in coefficients of eigenstates after diagonalizing the Hamiltonian. Let n be the eigenstate index of the active adibatic state. We choose a sign convention of $c_a^{(n)}(t)$ to be always non-negative throughout the adiabatic dynamics.

In the symmetry preserving method, the active state is always the lowest state ($n = 1$) in the modified Hamiltonian. Hence, choosing the sign of the lowest eigenstate of the Hamiltonian to be always positive conserves the phase of the active state. In the non-symmetry preserving overlap approach, the index n can change over time. To account for this, we multiply all eigenstates by either 1 or -1 that is consistent with our sign convention ($c_a^{(n)}(t) \geq 0$). For example, suppose that the overlap method detects a trivial crossing, and the eigenstate index of the active state changes from $n = 1$ at time t to $n = 2$ at time $t + \delta t$. If $|\Psi_k(t + \delta t)\rangle$ is the k-th eigenstate immediately coming out of the numerical eigensolver, we apply a phase projection,

$$|\Psi_k(t + \delta t)\rangle \rightarrow f_1 |\Psi_k(t + \delta t)\rangle \tag{S.17}$$

where

$$f_1 = \begin{cases} 1 & \text{if } c_a^{(2)} > 0, \\ \text{-1} & \text{if } c_a^{(2)} < 0, \end{cases} \tag{S.18}$$

where $c_a^{(2)}$ is the coefficient of the diabatic state $|\phi_a\rangle$ for $|\Psi_2(t + \delta t)\rangle$ (see Eq. S.15). An example trajectory from an actual simulation using this phase projection is demonstrated in Figure 5b in the main text.

In Figure S.3, we compare results with and without the phase conservation in the non-symmetry preserving method. We find that conserving the wavefunction phase has negligible effect on our simulations in terms of both exciton transport characteristics (Figure S.3a) and sizes of excitons (Figure S.3b). This may be due to the fact that each component of Hellmann-Feynman forces, $F_{\text{ex}}^{(n)}(\theta_i)$, in our model does not depend on the sign of a single coefficient, $b_i^n \equiv \langle i|\Psi_n\rangle$, but on the product of two adjacent coefficients, $b_i^{(n)} b_{i+1}^{(n)}$, as derived in Eq. 27 in the main text.

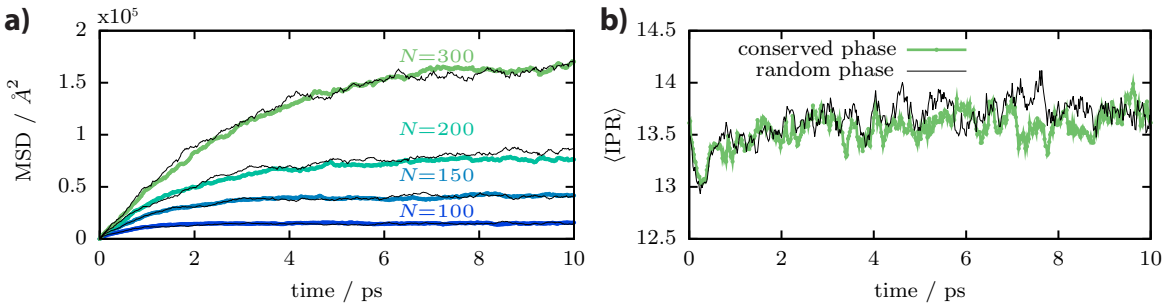

FIG. S.3. Phase conservation has negligible effect on non-symmetry preserving adiabatic dynamic simulations. (a) Mean-squared displacements (MSD) for excitons on polymer chains with varying number of monomer units. For each polymer size, data is averaged over 2000 independent trajectories initialized in the lowest exciton state. (b) Time evolution of the average inverse participation ratios (IPR) for 300-mer chains. Each data set represents an average over 3000 independent trajectories. In both panels, black curves are results from simulations where eigenstates at every timestep have random phases without properly accounting for sign changes. Blue to green colored curves are represent those after applying phase projections via Eq. S.17.

S.5. COMPARISON OF TRIVIAL CROSSING DETECTION SCHEMES

Figure S.4 compares two trivial crossing detection schemes: the joint probability density and the overlap integral. While the overlap method is able to detect trivial crossing for small diabatic coupling (*e.g.*, $|V_{ab}| < 0.5$ meV), it fails to detect crossing points when $|V_{ab}| \geq 0.5$ meV, whereas the joint probability density method succeeds in all cases.

S.6. PARAMETERIZATION OF EXCITON DYNAMICS MODEL OF CONJUGATED ORGANIC POLYMERS

A. Benchmark method: all-atom QCFF/PI

Coarse grained exciton transport model of conjugated organic polymer has been parameterized based on the QCFF/PI method,[2] which has been used to study singlet excited state dynamics of thiophene 30-mers in earlier work.[3] In QCFF/PI, the molecular system is partitioned into two subsystems: one containing explicit quantum mechanical detail and the other in which such details are accounted for implicitly. In our case, the quantum subsystem

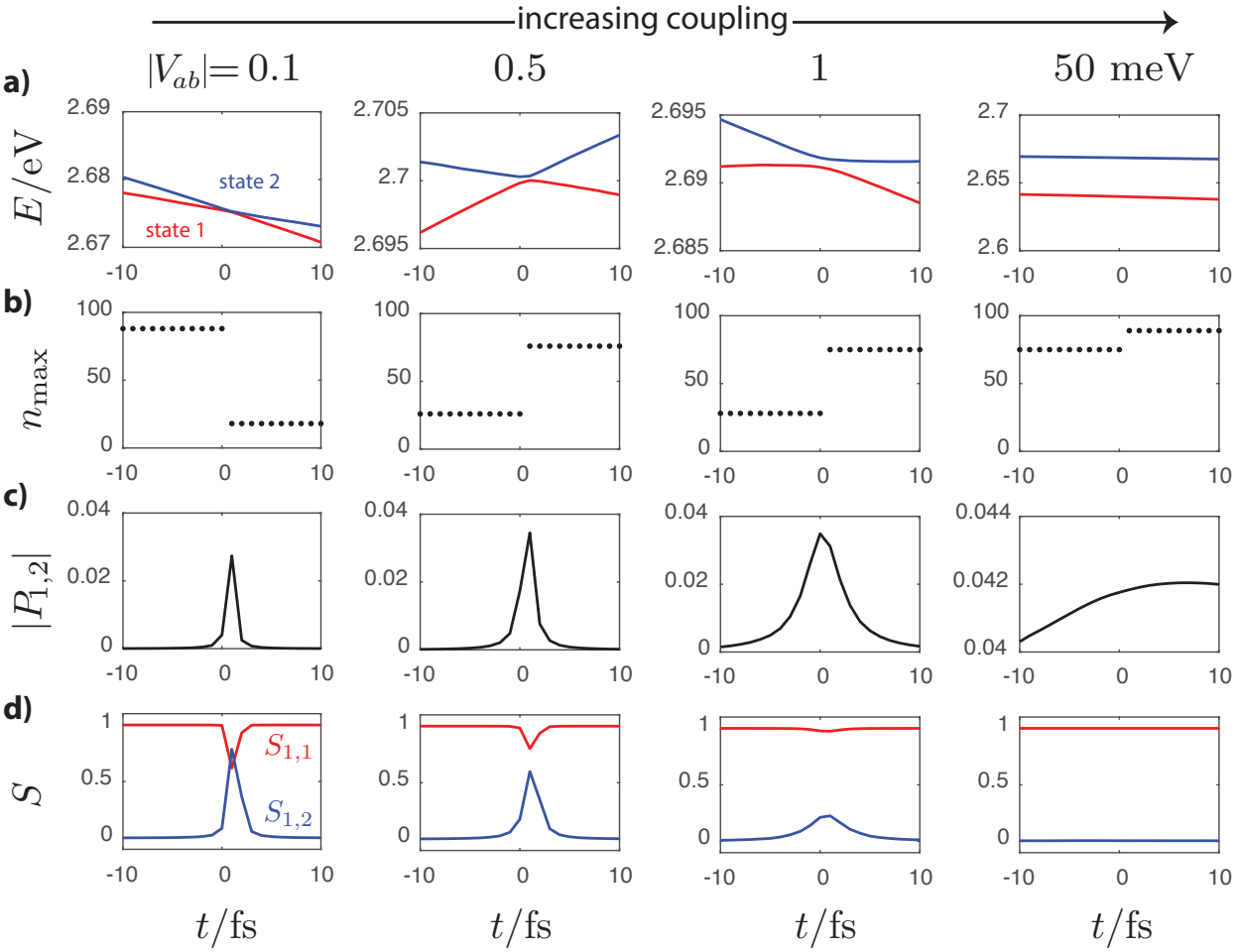

FIG. S.4. Case studies of crossing points with varying coupling strength between two diabatic states for a 100-mer linear organic conjugated polymer model. From left to right column, the coupling strength, $|V_{ab}|$, is increasing. Each row plots properties of the two lowest adiabatic states: (a) eigenvalues of states 1 and 2, E_i, (b) the monomer site index with maximum exciton density, $n_{\max}$, (c) joint exciton density of states 1 and 2, $P_{1,2}$, and (d) the overlap integral between states i and j, *i.e.*, $S_{i,j} = |\langle\psi_i(t)|\psi_j(t+\delta t)\rangle|$ with $\delta t = 1$ fs. In all plots, the time origin is defined to be the crossing point, t_c.

contains only the π-electrons, which are described using a semi-empirical Pariser-Parr-Pople (PPP) Hamiltonian.[4–6] All remaining degrees of freedom (nuclear as well as the core and sigma electrons) belong to the classical subsystem, which is modeled as a positively charged nuclear scaffold that evolves via a molecular mechanics force field. All calculations of electrostatic interactions here include the a uniform dielectric screening to approximately mimic the influence of a non-polar organic solvent. The particular value of the dielectric constant

used in this study is $\varepsilon_r = 2.7$.

Following the notation of Warshel and Karplus,[2] the molecular mechanics forcefield is given by

$$V_\sigma(r) = V_\sigma(r)_{\text{conj}} + V_\sigma(r)_{\text{sat-conj}}, \tag{S.19}$$

where the subscript *conj* refers to the collection of atoms participating in the conjguated π-electron system, and the subject subscript *sat-conj* refers to the interaction between the collections of saturated atoms (in this case, only hydrogen atoms) and conjugated atoms. The first term in the above equation is given by

$$\begin{aligned} V_\sigma(r)_{\text{conj}} = & \underbrace{\sum_i D_b \left(e^{2-\alpha(b_i-b_0)} - 2e^{2-\alpha(b_i-b_0)}\right)}_{\text{bonds}} + \underbrace{\frac{1}{2}\sum_i \left[K_\theta(\theta_i-\theta_0)^2 + F(q_i-q_0)^2\right]}_{\text{bond angles}} \\ & + \underbrace{\frac{1}{2}\sum_i \left[K_\phi^{(1)}\cos\phi_i + K_\phi^{(2)}\cos 2\phi_i\right]}_{\text{torsional angles}} + \underbrace{\sum_i K_{\theta\theta'}(\theta_i-\theta_0)(\theta_i'-\theta_0)\cos\phi_i}_{\text{angle dependent torsional angles}} \\ & + \underbrace{\sum_{ij}\left(Ae^{-\mu r_{ij}} - Br_{ij}^{-6}\right)}_{\text{non-bonded pairs}}, \end{aligned} \tag{S.20}$$

where b_i, θ_i, and ϕ_i represent the bond lengths, bond angles, and torsional angles, respectively; θ_i and θ_i' are two bond angles, XAB and ABY, of a bond AB; q_i is the distance between the first and the third of three consecutively bonded atoms; and r_{ij} is the distance between atoms i and j. The second term in Eq. S.19 is given by

$$\begin{aligned} V_\sigma(r)_{\text{sat-conj}} = & \underbrace{\frac{1}{2}\sum_i \left[K_b(b_i-b_0)^2 + 2D_b\right]}_{\text{bonds}} + \underbrace{\frac{1}{2}\sum_i \left[K_\theta(\theta_i-\theta_0)^2 + F(q_i-q_0)^2\right]}_{\text{bond angles}} \\ & + \underbrace{\frac{1}{2}\sum_i \left(K_\phi^{(2)}\cos 2\phi_i\right)}_{\text{dihedral}} + \underbrace{\sum_{ij}\left(Ae^{-\mu r_{ij}} - Br_{ij}^{-6}\right)}_{\text{non-bonded pairs}}. \end{aligned} \tag{S.21}$$

Forcefield parameters used in this study are listed in Table I.

Following the notation by Lobaugh and Rossky,[7,8] the electronic energy portion of the potential is given by the PPP method and is expressed as

$$V_\pi = \frac{1}{2}\sum_{\mu\nu} P_{\mu\nu}(H_{\mu\nu} + F_{\mu\nu}), \tag{S.22}$$

where the summation is over the atomic sites that contribute to the π-system (*i.e.*, Carbon and Sulfur). The terms $P_{\mu\nu}$, $F_{\mu\nu}$, and $H_{\mu\nu}$ are the bond-order, Fock, and one-electron core

TABLE I. Molecular Mechanics Forcefield Parameters

Bond	D_b (kcal mol^{-1})	$K_b/2$ (kcal mol^{-1} Å^{-2})	α (Å^{-1})	b_0 (Å)
C-C	87.94	-	1.786	1.46
C-S	65.00	-	1.700	1.78
C-H	103.10	339.00	1.080	-
Bond Angle	$K_\theta/2$ (kcal mol^{-1} rad^{-2})	θ_0 (rad)	$F/2$ (kcal mol^{-1} Å^{-2})	q_0 ($\AA$)
C-C-C	52.8	2.094	32.05	2.56
C-C-S	50.0	2.094	30.40	2.90
C-S-C	50.0	2.094	30.40	2.50
C-C-H	24.0	2.094	29.535	2.178
S-C-H	15.0	2.094	26.50	2.18
Torsional Angle	$K_\phi^{(1)}/2$ (kcal mol^{-1})	$K_\phi^{(2)}/2$ (kcal mol^{-1})	$K_{\theta\theta'}$ (kcal mol^{-1} rad^{-2})	
X-C-C-X	2.3	2.54	-6.0	
X-C-S-X	2.3	4.5	-10.0	
X-C-H-X	-	0.8	-	
Non-bonded	A (kcal mol^{-1})	B (kcal mol^{-1})	μ (Å^{-1})	
C$\cdots$C	11392.84	560.44	3.0115	
S$\cdots$S	30923.41	1521.19	3.0115	
H$\cdots$H	4882.64	26.59	4.3458	
C$\cdots$S	18769.80	923.33	3.0115	
C$\cdots$H	7458.36	134.97	3.5577	
S$\cdots$H	12287.72	222.36	3.5577	

matrix elements, respectively. The bond-order matrix elements are given by

$$P_{\mu\nu} = 2\sum_{i}^{n} c_\mu^i c_\nu^i, \tag{S.23}$$

where the product of molecular orbital coefficients c_μ^i and c_ν^i at site μ and ν is summed over occupied molecular orbitals ($n = 3N$ for N-mer polythiophene). The Fock matrix elements

are

$$F_{\mu\nu} = H_{\mu\nu} - \frac{1}{2}P_{\mu\nu}\gamma_{\mu\nu} \text{ if } \mu \neq \nu$$
$$F_{\mu\mu} = H_{\mu\mu} + \frac{1}{2}P_{\mu\mu}\gamma_{\mu\mu} + \sum_{\rho\neq\mu} P_{\rho\rho}\gamma_{\mu\rho}. \tag{S.24}$$

$\gamma_{\mu\nu}$ are the two-electron repulsion matrix elements, which are in turn defined as

$$\gamma_{\mu\nu} = \frac{e^2}{R_{\mu\nu} + a_{\mu\nu}}, \tag{S.25}$$

where

$$a_{\mu\nu} = \frac{2e^2}{\gamma_{\mu\mu} + \gamma_{\nu\nu}}, \tag{S.26}$$

e is the magnitude of the electron charge, $R_{\mu\nu}$ is the distance between atoms μ and ν, and $\gamma_{\nu\nu}$ is the one-center repulsion parameter. The diagonal elements of the one-electron core matrix are

$$H_{\mu\mu} = \alpha_\mu - \sum_{\rho\neq\mu} Z_\rho\gamma_{\mu\rho}, \tag{S.27}$$

where α_μ is the energy of the orbital μ. The second term is the interaction of the electron (at site μ) with the nuclear core (at site ρ), which has formal charge Z_ρ (equal to the number of 2p electrons the atom donates to the π-system). The off-diagonal elements of the one-electron core matrix are

$$H_{\mu\nu} = \beta_{\mu\nu} \quad \text{if } \mu \text{ and } \nu \text{ are covalently bonded,}$$
$$H_{\mu\nu} = 0 \qquad \text{otherwise } (\mu \neq \nu), \tag{S.28}$$

where β is the resonance parameter given by[7]

$$\beta_{\mu\nu} = [\beta_1^{\mu\nu} + \beta_2^{\mu\nu}(R_{\mu\nu} - R_{\mu\nu}^{\text{eq}})]e^{-\mu_{\mu\nu}(R_{\mu\nu}-R_{\mu\nu}^{\text{eq}})}. \tag{S.29}$$

The parameters for the PPP Hamiltonian that are used in this study are tabulated in Table II. Electronic excited states are computed using configuration interaction with single excitations (CIS).

B. Ground state coarse grained model parameterization

Ground state torsional dihedral angle potential energy, U_{g}, for thiophene rings has been parameterized from QCFF/PI simulations in the ground state of quaterthiophene at $T =$

TABLE II. PPP Hamiltonian Parameters

Site	$\gamma_{\mu\mu}$ (hartree)		$\alpha_{\mu\nu}$ (hartree)	
C	0.3895		-0.42078	
S	0.3598		-0.734986	
Bond	$\mu_{\mu\nu}$ (bohr^{-1})	$\beta_1^{\mu\nu}$ (hartree)	$\beta_2^{\mu\nu}$ (hartree bohr^{-1})	$R_{\mu\nu}^{\mathrm{eq}}$ (bohr)
C-C	0.73868	-0.089586	-0.019198	2.639948
C-S	0.81325	-0.078013	0.025506	2.66941

TABLE III. Ground state torsional potential coefficients

i	a_i (eV)	b_i (eV/deg)	c_i (rad)
1	0.02831	0.00465	1.571
2	0.01993	0.03616	-1.571
3	0.01626	0.06993	1.571

300 K. The ground state potential energy is parameterized from the potential of mean force (PMF) of torsional angles, *i.e.*, PMF $= -k_{\mathrm{B}}T \ln P(\theta)$, where $P(\theta)$ is the probability distribution of torsional angles based on the statistics of the middle bond torsional angle of each ground-state quaterthiophene at $T = 300$ K with a sample size of 100 equilibrated configurations. We fit the PMF to a Fourier series of the form to approximate U_{g},

$$U_g(\theta) = \sum_{i=1}^{3} a_i \sin\left(b_i\theta + c_i\right), \tag{S.30}$$

where the coefficients a_i, b_i, and c_i are tabulated in Table III.

To analyze dynamical properties of torsional modes, we compute the ring-ring planarity time correlation function,

$$C(t) = \frac{\langle \delta A(t)\delta A(0)\rangle}{\langle \delta A(0)^2}, \tag{S.31}$$

$$\delta A(t) = |\cos\theta(t)| - |\cos\theta|_{\mathrm{avg}}, \tag{S.32}$$

where $|\cos\theta|_{\mathrm{avg}}$ is the average value of $\cos\theta$ of a given trajectory. The pair of angle brackets in Eq. S.31 represents an ensemble average over all 100 trajectories. We have generated a hundred 10 ps-long equilibrated trajectories of quaterthiophene.

The moment of inertia (I) and frictional damping coefficient (η) of torsional modes in the coarse grained Langevin model are chosen by fitting $C(t)$ generated by the coarse grained

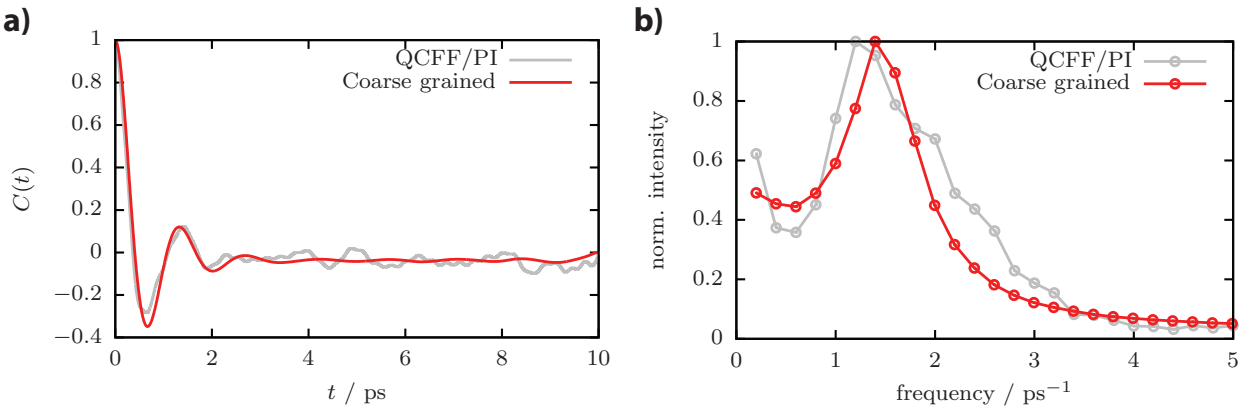

FIG. S.5. Comparisons of the ground state time correlation function (a) and its Fourier transform (b) generated from two different methods: the atomistic QCFF/PI method (gray lines) and the coarse-grained Langevin model (red lines). QCFF/PI results have been averaged over 100 trajectories of quarterthiophene, each 10 ps long. The coarse grained model parameters are $U_g(\theta)$ (Eq. S.30), $I = 3.0$ eV fs^2 deg^{-2}, $\eta = 0.0035$ eV fs deg^{-2}, and $T = 300$ K.

model to those of the QCFF/PI method. The results from the coarse grained Langevin model have been averaged over 1000 trajectories of linear quarterthiophene. The QCFF/PI data and the final fitting results are shown in Figure S.5. The resulting best fit parameters are $I = 3.0$ eV fs^2 deg^{-2} and $\eta = 0.0035$ eV fs deg^{-2}, which are the values used for all simulations reported in this work.

C. Frenkel exciton Hamiltonian parameterization

Excited state parameters in the Frenkel exciton Hamiltonian are determined based on the excited state QCFF/PI simulations of 30-mer polythiophene at $T = 300$ K. Starting from a linear polythiophene chain, we equilibrate its structure in the electronic ground state for 100 ps. We then turn on the excited state force in the lowest excited state to sample 100 configurations of 3 ps-long excited state dynamics.

To compute the through-bond coupling term J_{SE}, we project the excited state force acting on each atoms along the ring-ring torsional coordinate to compute $F_{\mathrm{ex}}(\theta_i)$, which is the torque acting on the i-th ring junction. We also compute the exciton density across each ring junction, ρ_i, by taking the overlap of electron and hole wavefunctions of all atoms in each ring connected to the i-th junction. The average value of $F_{\mathrm{ex}}(\theta_i)/\rho_i$ computed from

the QCFF/PI method is shown in Figure S.6a. We fit the average force from the QCFF/PI method to an analytical expression of the excited state force that we have derived based on the Frenkel exciton Hamiltonian model,

$$F_{\mathrm{ex}}(\theta_i) = 2J_{\mathrm{SE}} \sin(2\theta_i)\rho_i, \tag{S.33}$$

in which the only free-parameter during the fitting procedure is J_{SE}. From this approach, we obtain $J_{\mathrm{SE}} = -0.50 \pm 0.04$ eV. The resulting fit is also depicted as a red curve in Figure S.6a.

We estimate the transition dipole coupling magnitude, μ_0, by performing the coarse grained model simulations of 30-mer polythiophene in a linear configuration with varying values of μ_0. We compare the distribution of inverse participation ratio (IPR) of the lowest exciton state calculated from the coarse grained model to that of the QCFF/PI method. We find that $\mu_0 = 9.0$ D best reproduces the distribution obtained from QCFF/PI method (see Figure S.6b).

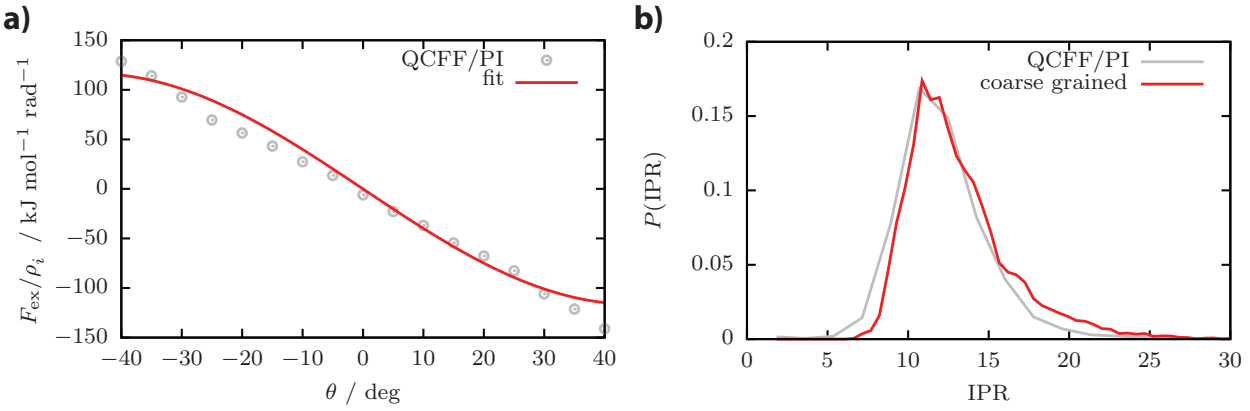

FIG. S.6. Benchmarking excited state properties to the atomistic QCFF/PI simulations. Panel (a) shows the excited state torque acting on ring junctions, normalized by the exciton density across those ring junctions. The red curve in panel (a) is the best fit result to the QCFF/PI data using Eq. S.33. Panel (b) plots the probability distribution of exciton sizes, quantified by the inverse participation ratio (IPR). The coarse grained model data are computed over 100 equilibrium torsional configurations of a 30-mer thiophene in the ground electronic state at $T = 300$ K.

S.7. SIMULATION OF CONJUGATED ORGANIC POLYMERS WITH CONFORMATIONAL DISORDER

The solution phase structure of 110-mer polythiophene is simulated using molecular dynamics of a coarse-grained polymer model of poly(3-hexylthiophene) (P3HT) developed by D. Huang *et al.*[9] Simulations have been carried out at constant volume and temperature using Langevin dynamics, starting from an initial configuration of randomly placed and oriented chain with intermonomer dihedral angles selected from a Boltzmann distribution of the intermonomer torsional potential. The temperature and friction coefficient are set to $T = 300$ K and $\gamma = (180 \text{ fs})^{-1}$, respectively. We have generated 300 disordered backbone conformations, each resulting from a 50 ns-long equilibration run. The average radius of gyration of these polymers is $R_g = 6.4 \pm 2.4$ nm.

To compute exciton diffusion coefficient in Frenkel exciton coarse grained model, we have sampled 200 independent trajectories per backbone conformation, resulting in 60,000 trajectories in total. We follow the same procedure of equilibrating the ground state torsional configurations as in the linear chain conformation. We then perform excited state dynamics in the lowest exciton state for 10 ps with $V_c = 10$ meV and the quenching boundary conditions as we have done for linear chains. We find that the average exciton diffusion coefficient for disordered backbone conformations is $D = 0.001 \pm 0.0002$ cm^2/s.

---

* awillard@mit.edu

[1] Van Voorhis, T.; Kowalczyk, T.; Kaduk, B.; Wang, L.-P.; Cheng, C.-L.; Wu, Q. *Annu. Rev. Phys. Chem.* **2010**, *61*, 149–170.

[2] Warshel, A.; Karplus, M. *J. Am. Chem. Soc.* **1972**, *94*, 5612–5625.

[3] Hu, Z.; Willard, A. P.; Ono, R. J.; Bielawski, C. W.; Rossky, P. J.; Vanden Bout, D. A. *Nat. Commun.* **2015**, *6*, 8246.

[4] Pariser, R.; Parr, R. G. *J. Chem. Phys.* **1953**, *21*, 466–471.

[5] Pariser, R.; Parr, R. G. *J. Chem. Phys.* **1953**, *21*, 767–776.

[6] Pople, J. A. *Trans. Faraday Soc.* **1953**, *49*, 1375–1385.

[7] Lobaugh, J.; Rossky, P. J. *J. Phys. Chem. A* **1999**, *103*, 9432–9447.

[8] Lobaugh, J.; Rossky, P. J. *J. Phys. Chem. A* **2000**, *104*, 899–907.

[9] Schwarz, K. N.; Kee, T. W.; Huang, D. M. *Nanoscale* **2013**, *5*, 2017–2027.